Diamond & Related Materials 131 (2023) 109566

Contents lists available at ScienceDirect

Diamond & Related Materials

journal homepage: www.elsevier.com/locate/diamond

Interface matters - Effects of catalyst layer metallurgy on macroscale morphology and electrochemical performance of carbon nanofiber electrodes

Ishan Pande [a], Laura Ferrer Pascual [a], Ayesha Kousar [a], Emilia Peltola [a,b], Hua Jiang [c], Tomi Laurila [a,d,*]

[a] Department of Electrical Engineering and Automation, School of Electrical Engineering, Aalto University, PO Box 13500, 00076 Aalto, Finland
[b] Department of Mechanical and Materials Engineering, Faculty of Technology, University of Turku, Vesilinnantie 5, 20500 Turku, Finland
[c] Department of Applied Physics, School of Science, Aalto University, PO Box 15100, 00076 Aalto, Finland
[d] Department of Chemistry and Materials Science, School of Chemical Engineering, Aalto University, PO Box 16200, 00076 Aalto, Finland

ARTICLE INFO

Keywords:
Carbon nanomaterials
Chemical vapor deposition
Phase diagram
Cyclic voltammetry

ABSTRACT

The effect of catalyst materials and different process parameters on the growth of carbon nanofibers (CNFs) has been widely investigated. Typically, an adhesion metallization is required together with the catalyst to secure adequate attachment to the surface. The interactions within this multilayer structure and their effect on CNF growth and morphology has, however, not been thoroughly assessed. Thus, this work presents the growth behavior, the macroscale morphology, and the basic electrochemical characteristics of CNFs grown on two types of substrates - (1) Si + 80 nm Cr + 20 nm Ni, and (2) Si + 20 nm Ti + 20 nm Ni. Our results show that the macroscale geometric parameters of CNFs can be readily altered by using different adhesive layers. The inherently unstable Ti-Ni interface results in diffusion of Ni towards the silicon wafer to form silicide, which reduces the amount of available Ni for CNF nucleation, and therefore, the population density of fibers is reduced. On the other hand, the Cr-Ni interface results in a larger population density, but the rate of growth is reduced due to diffusion of carbon into the thicker Cr layer. The results are rationalized by using relevant binary and ternary phase diagrams. Further, cyclic voltammetry experiments show that the pseudocapacitance of CNFs shows a correlation with the length and population density of fibers, while the electron transfer kinetics appear nearly reversible for all the electrodes. This simple approach can be used for tailoring CNFs for specific applications by controlling their macroscale geometrical parameters.

1. Introduction

Carbon nanofibers (CNFs) have attracted considerable attention in a wide variety of applications, including biosensing [1], energy storage [2], water purification [3] and catalysis [4]. CNFs are cylindrical nanostructures that consist of stacked graphene sheets of various sizes and orientations. Their length may vary from tens to hundreds of nanometers, while their diameter may reach up to tens of micrometers. CNFs possess a large surface area which can be functionalized with a variety of chemical species. In addition, CNFs have high electrical conductivity, which makes them ideal candidates for electrochemical biosensing [5–7].

CNFs can be grown using a variety of techniques, including electrospinning [8], chemical vapor deposition (CVD) [9] and hot filament assisted sputtering [10]. Plasma enhanced CVD (PECVD) is a widely used method for growing vertically aligned CNFs (VACNFs) at relatively low temperatures. A PECVD growth process for CNFs typically involves a carbonaceous gas (e.g. C_2H_2, C_2H_4) and an etchant gas (e.g. NH_3 or H_2), which are activated in a glow discharge. The growth of CNFs occurs through the nucleation of a nanoscale metal catalyst layer (e.g. Ni, Fe, Pd or Pt) [11]. An adhesive layer (e.g. Ti, Cr, W) is often deposited between the substrate and the catalyst layer, in order to prevent the intermixing of the catalyst and substrate materials.

The microstructure and macroscale morphology of CNFs depend on

* Corresponding author at: Department of Chemistry and Materials Science, School of Chemical Engineering, Aalto University, PO Box 16200, 00076 Aalto, Finland.
E-mail address: tomi.laurila@aalto.fi (T. Laurila).

https://doi.org/10.1016/j.diamond.2022.109566
Received 20 July 2022; Received in revised form 25 October 2022; Accepted 18 November 2022
Available online 22 November 2022

the process parameters, e.g. temperature, time, gas flow, reactor pressure and plasma power. Moreover, the composition and thickness of adhesive and catalyst layers also affect these properties. These effects have been reported in various studies. For example, Melechko et al. demonstrated that CNF growth mode changes from tip-type to base-type by changing the flow ratio of carbonaceous and etchant gases in the PECVD process [12]. Röthlisberger et al. documented the effects of Ni layer thickness on bidirectional growth of CNFs (i.e. both tip-type and base-type simultaneously) [13]. Merkulov et al. reported the growth of individual VACNFs by controlling the size of catalyst layer dots, using Ni as the catalyst layer and Ti as the adhesive layer [14].

An aspect of the reaction that is often overlooked is the interaction between the substrate, catalyst and adhesive layers. To the best of our knowledge, this phenomenon has not been systematically investigated. Furthermore, many studies on electrochemical biosensing of electrodes do not address the effects of well controlled macroscale geometrical parameters – length, diameter, population density, etc. – on the performance of the electrode.

In this paper, we report PECVD growth of CNFs on two types of substrates – 80 nm Cr + 20 nm Ni and 20 nm Ti + 20 nm Ni (hereafter referred to as Cr-Ni and Ti-Ni, respectively). For each substrate type, we prepared four sets of CNF samples by varying the growth time (1, 5, 10 and 30 min), while the other growth parameters were kept constant. We studied the differences in macroscale geometry between the CNFs prepared under these conditions using scanning electron microscopy (SEM). We used phase diagrams and thermodynamics combined with detailed transmission electron microscopy (TEM) study to rationalize the differences between CNFs grown on the two types of substrates. Finally, we investigated basic electrochemical properties of each type of CNF, and rationalized the effects of macroscale morphology on pseudocapacitance and electrochemical windows of the CNFs.

2. Methods

p-type Silicon wafers (Siegert Wafers, Germany) were used as substrates for all the samples. First, the wafers were coated with adhesive and catalyst metal layers – 20 nm Ti followed by 20 nm Ni for Ti-Ni-CNFs, and 80 nm Cr followed by 20 nm Ni for Cr-Ni-CNFs. An electron beam evaporator (MASA IM-9912) was used for depositing metal layers. The chamber pressure was approximately 2×10^{-7} mbar during evaporation. Subsequently, the wafers were cleaved into smaller pieces, measuring approximately 7 mm × 7 mm. Finally, CNF growth was carried out using a PECVD reactor (Aixtron Black Magic).

The PECVD process was carried out as follows: First, the chamber was pumped down to 0.1 mbar. Then, the chamber was heated to 400 °C with a ramp speed of approximately 250 °C per minute. When the temperature reached 395 °C, the chamber was injected with a 100 sccm NH_3 buffer. The ramp rate was then increased to 300 °C per minute and the chamber was heated up to 600 °C. When the temperature reached 575 °C, 230 W DC plasma was ignited. 30 sccm C_2H_2 was simultaneously injected into the chamber, while the flow rate of NH_3 was increased to 125 sccm. These parameters were maintained for 1, 5, 10 or 30 min, in order to prepare CNFs of four different lengths. The chamber pressure was approximately 3 mbar during the growth process.

CNF morphology and geometry were studied using SEM (Zeiss Supra 40 and Zeiss Sigma VP). Length, diameter and area analyses were carried out using imageJ. We estimated the average length and diameter by measuring 20 CNFs from the cross-sectional SEM images (Fig. 1). Area analysis was carried out as follows: Area covered by Ni was highlighted by applying brightness/contrast and threshold settings to the top-view SEM images of 1 min grown CNF samples (Fig. S2). The percentage of white pixels, which corresponds to Ni, was then estimated using imageJ software. An area of 7000 nm × 4800 nm was used in this analysis. While a more detailed analysis would be required to obtain precise quantitative values, our analysis is sufficient to demonstrate that there is a significant difference between the two substrates.

TEM imaging was performed on a Jeol JEM 2200FS TEM equipped with an X-ray energy dispersive spectrometer (EDS). Cross-sectional TEM samples were prepared by EAG Laboratories (USA) using a focused ion beam (FIB). Sputtered carbon was used as the filler material. The sample was coated locally at the cross-section site with two additional layers of carbon.

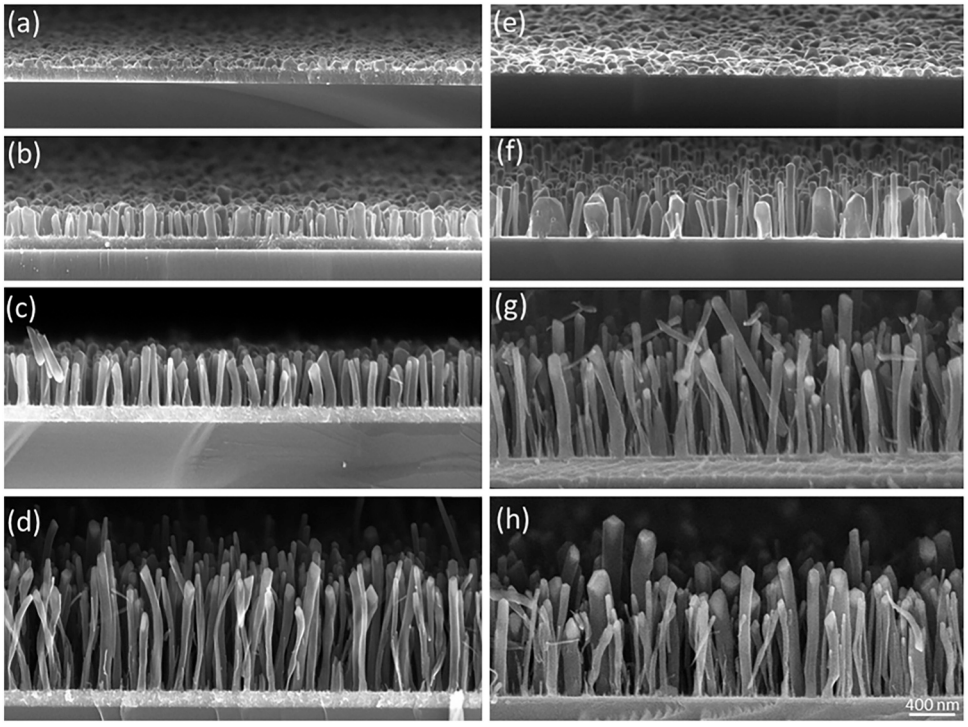

Fig. 1. Cross-sectional SEM images of CNFs grown on Cr-Ni substrates for (a) 1 min, (b) 5 min, (c) 10 min, (d) 30 min; and on Ti-Ni substrates for (e) 1 min, (f) 5 min, (g) 10 min, (h) 30 min.

Binary phase diagrams (Figs. 4, S6) were generated using FactSage Education 8.1 Package. FactSage is a fully integrated database computing system in chemical thermodynamics and consists of a variety of information, database, calculation and manipulation modules that access various pure substances and solution databases [15].

Cyclic voltammetry was performed with a Gamry Reference 600 potentiostat and Gamry Framework software in a three-electrode setup with a Ag/AgCl as reference electrode and a Pt wire as the counter electrode. The solutions were purged with nitrogen gas for at least 15 min. The potential window measurements were done in 0.15 M H_2SO_4 and PBS pH 7.4 (NaCl (137 mM), KCl (2.7 mM), Na_2HPO_4 (10 mM), and KH_2PO_4 (1.8 mM)). The outer-sphere redox (OSR) probe was 1 mM $Ru(NH_3)_6^{2+/3+}$ prepared from hexaamminer-uthenium(III) chloride (Sigma-Aldrich) dissolved in 1 M KCl (Merck Suprapur).

3. Results and discussion

SEM images presented in Fig. 1 demonstrate the effect of growth duration on the length of CNFs on Cr-Ni and Ti-Ni substrates. Measured values are presented in Fig. 2 and Table 1. There is a significant difference between the evolution of length in both types of substrates. Samples grown for 1 min do not contain nanofibers – instead, we observe the initial stages of CNF nucleation. There are notable differences between Cr-Ni and Ti-Ni substrates already at this stage (Fig. 3), which we elaborate below.

At 5 min, CNFs are clearly visible in both the substrates. On Cr-Ni substrates, the average length of CNFs is approximately 221 nm, while on Ti-Ni substrates, the average length is considerably larger - 361 nm. After 10 min of growth, the corresponding values are 415 nm and 774 nm, respectively. After 30 min, however, the CNF lengths on both substrates are similar - 915 nm and 873 nm, respectively. Thus, the rate of CNF growth is lower in Cr-Ni substrates compared to Ti-Ni substrates up to 10 min. Interestingly, the length seems to saturate at <1 μm for both substrates. Moreover, CNFs grown on Cr-Ni substrates have a narrower distribution of length, i.e., they are more uniform in length. The average diameters of CNFs do not differ significantly between the two substrates. The average diameters also remain similar for different growth duration (approx. 70 nm). However, Ti-Ni-CNFs have a wider distribution of diameters.

It should be noted that measuring the average dimensions of CNFs is not straightforward. The longer CNFs are curved, and their diameters are not strictly identical along the entire length. Moreover, the smaller CNFs are likely to be obstructed by larger ones in the SEM micrographs. However, we believe that the values presented in this work provide a qualitative comparison between different batches.

SEM images presented in Fig. 3 demonstrate the difference between the population density of fibers grown on Cr-Ni and Ti-Ni substrates. The nucleation of Ni film occurs differently in both types of substrates. On the Cr-Ni substrate, we observe that the Ni film breaks down into particles of more uniform size. Moreover, a larger proportion of the surface is covered with Ni nanoparticles. On the other hand, on the Ti-Ni substrate, we see a less even distribution of Ni nanoparticles. Moreover, a smaller proportion of the surface is covered with Ni. In the Cr-Ni substrate, 50.04 % of the visible surface is covered with Ni, whereas the corresponding value for Ti-Ni substrate is only 37.13 % (Fig. S2, Table 1). Fig. 3 and Table 1 support our observations from Fig. 1, that CNFs grown on Cr-Ni substrates have a narrower distribution of length and diameter. A similar analysis could not be carried out for the 5-, 10- and 30-min grown samples because longer CNFs partially obstruct the underlying surface.

We can safely assume that the entire Ni film is nucleated in the early stages of the reaction, therefore, the population density of CNFs remains the same across the four growth times (1, 5, 10 and 30 min). Thus, even though lengths of CNFs grown for 30 min are similar for both substrates, we observe a greater population density of CNFs in Cr-Ni substates. This results in a larger surface area, and hence a larger pseudocapacitance as discussed below.

In addition to the reaction between the carbon source and the catalyst layer that has been extensively studied [14,16–18], the much less investigated interaction between the catalyst and adhesive layers also has a significant role in the CNF growth process. To rationalize interfacial effects, we use binary and ternary phase diagrams that are available in the literature (see below) and the concept of local equilibrium at

Table 1
Measured values of CNF length, diameter, and percentage of surface covered by Ni. Sample size = 20.

Sample type	CNF length (nm)	CNF diameter (nm)	% of surface covered by Ni
Cr-Ni-CNF 1 min	N/A	N/A	50,04 %
Ti-Ni-CNF 1 min	N/A	N/A	37,13 %
Cr-Ni-CNF 5 min	221 ± 61	71 ± 49	N/A
Ti-Ni-CNF 5 min	361 ± 131	66 ± 51	N/A
Cr-Ni-CNF 10 min	415 ± 86	65 ± 17	N/A
Ti-Ni-CNF 10 min	774 ± 217	88 ± 29	N/A
Cr-Ni-CNF 30 min	915 ± 257	69 ± 27	N/A
Ti-Ni-CNF 30 min	873 ± 181	84 ± 43	N/A

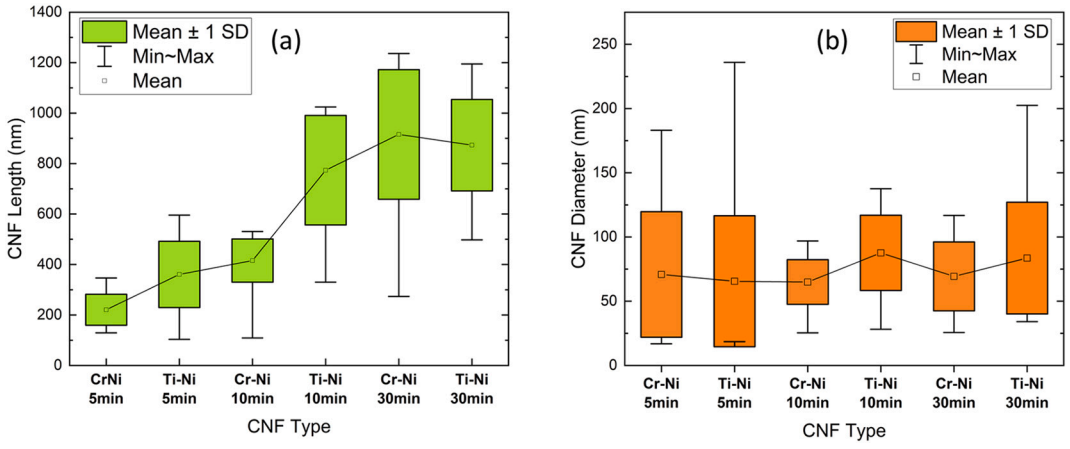

Fig. 2. Comparison of lengths (a) and diameters (b) of CNF samples. Sample size = 20.

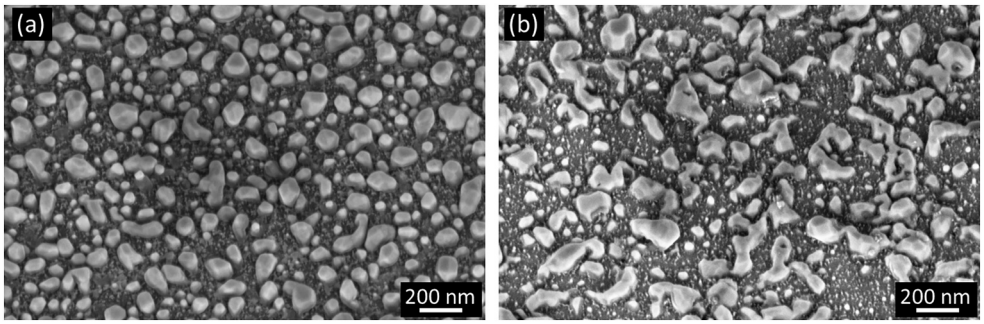

Fig. 3. SEM images of CNFs grown for 1 min on a Cr-Ni substrate (a), and a Ti-Ni substrate (b). The SEM stage was tilted by 25^0.

the interfaces between the phases. Local equilibrium is defined so that the equilibrium exists only at the interfaces between the different phases present in the system. This means that the thermodynamic functions are continuous across the interface, and the compositions of the phases right at the interface are very close to those indicated by the equilibrium phase diagram. This also indicates that there are activity gradients in the adjoining phases. These gradients, together with the diffusivities, determine the diffusion of components in the various phases of a joint region. This concept is different from the assumption of global equilibrium, where it is assumed that the system's Gibbs free energy (G) function has reached its global minimum value and then, the system is in mechanical, thermal, and chemical equilibrium with its surroundings. Consequently, there are no gradients inside the individual phases, and no changes in the macroscopic properties of the system are to be expected.

Binary phase diagrams of the Ni-Ti and Ni-Cr systems (Fig. 4) provide us information about the equilibrium phases present in these systems at different temperatures. Phase diagrams do not provide any information about the kinetics of these reactions or the spatial distribution of the phases. However, they provide a useful framework for comparing the two systems, and especially for ruling out thermodynamically impossible phases [19].

In the Cr-Ni phase diagram (Fig. 4(a)), there are no intermetallic compounds that are stable at 600 °C. Based on the assumption that local equilibrium is established in the system, we can see that at this temperature, stable phases are BCC_A2 (i.e. BCC Cr), BCC_A2 + FCC_A1, and FCC_A1 (i.e. FCC Ni). In addition, whereas the solubility of BCC Cr is very high to FCC Ni, the solubility of FCC Ni to BCC Cr is orders of magnitude smaller. Therefore we expect that most of the Ni would remain unreacted and available for CNF catalysis, at the growth temperature (600 °C). This is consistent with the observation of the relatively high population density of fibers grown on Cr-Ni substrate compared to Ti-Ni substrate (Fig. 3). However, at lower temperatures, $CrNi_2$ is stable as well. Hence, if the ramp rate is low, it is possible that intermetallic compound $CrNi_2$ would start to form during ramping, which would reduce the amount of Ni that is available for CNF growth. This explains the significantly lower population density of fibers on Cr-Ni substrate at a low ramp rate (Fig. 5).

TEM micrograph shown in Fig. 6 as well as the associated EDX analyses (Fig. S3) provide strong evidence for the above reasoning. We can see that the interface after the CNF growth consists of Cr with some dissolved graphite and/or chromium carbide, and there is practically no Ni left at the interface. There are also no intermetallic layers visible at the interfacial area consistent with the binary phase diagram.

On the other hand, the Ti-Ni system contains several intermediate phases at 600 °C (Fig. 4(b)). Thus, at equilibrium, we expect the formation of Ti_2Ni, $TiNi_3$, α-Ti and Ni. Even though our system is not at equilibrium (precursor gases and plasma are injected into the system after a few minutes of ramping), we can reasonably assume that a significant part of Ni reacts with Ti or diffuses through the Ti layer towards the Si substrate. The latter is driven by the fact that Ni has a high affinity for forming silicide [20] (Fig. S6). Thus, the more thermal energy we provide to the system, the less Ni will be available for CNF formation. The following observations support this hypothesis: (1) When we decrease the ramp rate, there is no CNF growth on Ti-Ni substrates. (2) If we add a pre-annealing step in the recipe, we get no CNF growth (some samples still result in growth under these conditions, but the vast majority do not). (3) CNF growth on Ti-Ni substrate is not very repeatable. On the other hand, Cr-Ni substrates resulted in uniform CNF growth across multiple batches. Finally, (4) the TEM cross-section (Fig. 6)

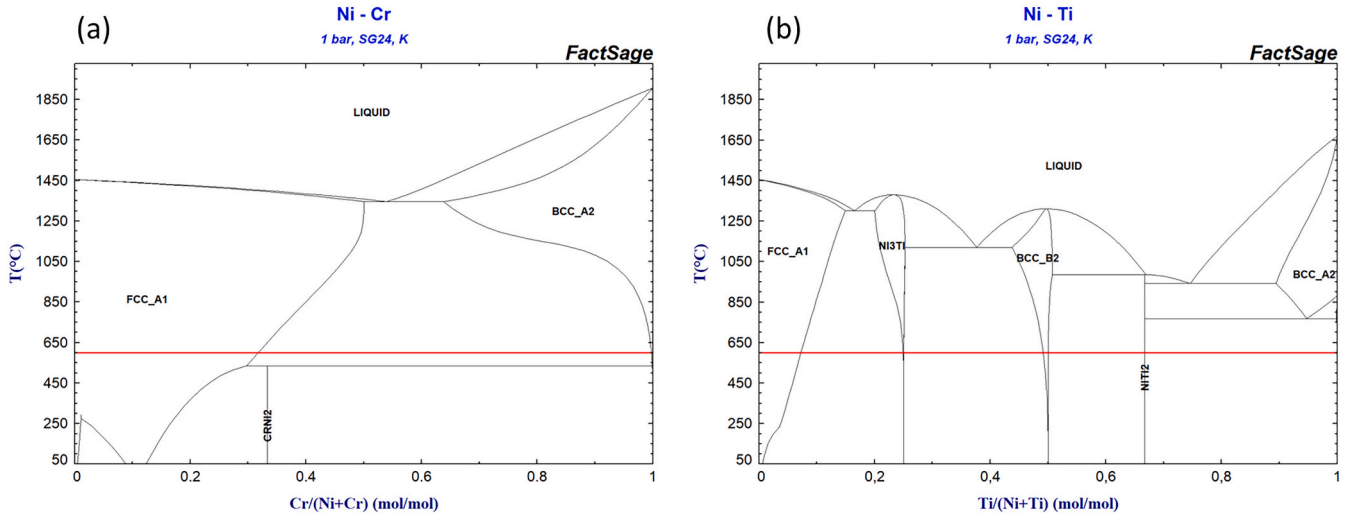

Fig. 4. Binary phase diagrams of the Cr-Ni (a) and Ti-Ni (b) systems [15]. The red lines correspond to our process temperature, 600 °C.

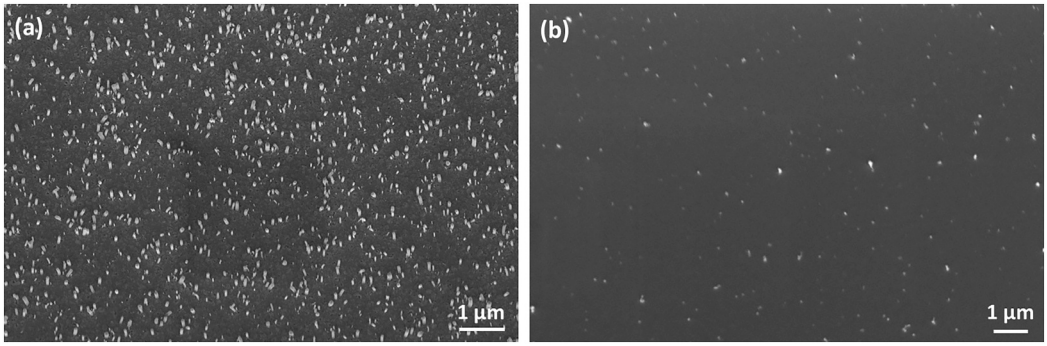

Fig. 5. SEM images of CNF samples grown for 5 min with low ramp rate (100 °C per minute) on Cr-Ni substrate (a) and Ti-Ni substrate (b). The Cr-Ni substrate appears to have CNF growth with a significantly lower population density, while the Ti-Ni substrate has almost no visible fibers.

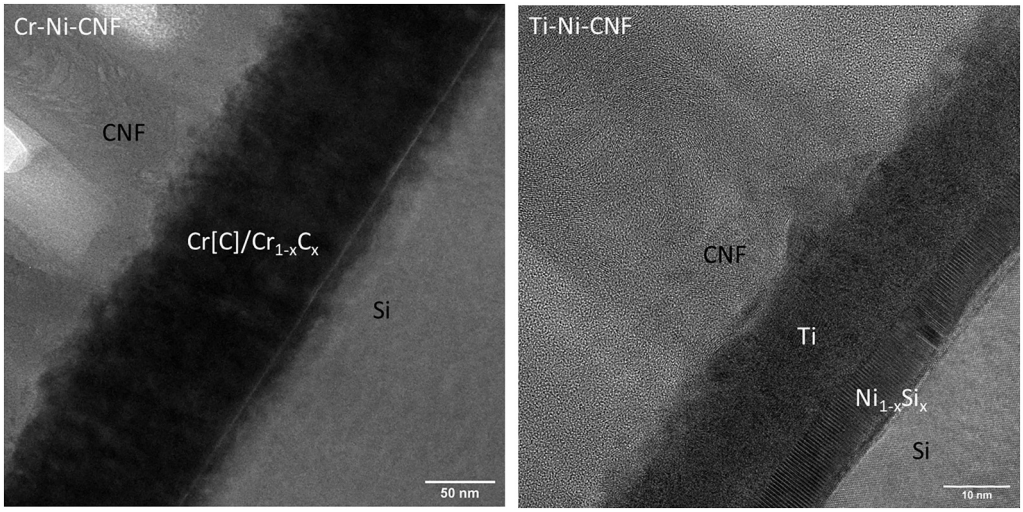

Fig. 6. TEM images of fiber-substrate interfaces along with probable phases. EDS data of the interfacial layers are presented in Fig. S3. TEM cross sections were prepared from 10 min-grown CNFs.

clearly shows the formation of an intermediate reaction layer at the Ti/Si interface, which contains significant amounts of Ni.

Fig. 2 shows that 5 min and 10 min Cr-Ni-CNFs are considerably shorter than their Ti-Ni counterparts, while they reach similar lengths after 30 min. Can we somehow rationalize this observation based on the thermodynamics and kinetics of the system? One important factor is the dissolution of carbon into the underlying metal layers. Our EDS scans indicate the presence of carbon in both Cr and Ti underlayers (Fig. S3). But what are the differences? Firstly, the 80 nm thick Cr layer is likely to dissolve significantly more carbon than the 20 nm thick Ti layer simply owing to its higher overall volume. Secondly, based on the diffusion coefficients calculated from the diffusion couple experiments [Cr,Ti] the intrinsic diffusion coefficient of carbon in Cr is slightly smaller than that of Ti, indicating that it will likely take considerably more time for carbon to reach the Cr/Si than the Ti/Si interface. In fact, there is a clear carbon peak at approximately the midpoint of the Cr layer (Fig. S3(c)), while there is no carbon peak at the Cr-Si interface (Fig. S3(d)). This clearly indicates that carbon has not yet reached the bottom of the Cr layer. On the other hand, there is a clear carbon peak at Ti layer as well as the Ni-silicide layer below it (Fig. S3(e, f)), which indicates that carbon has diffused throughout the underlayer already after 10 min of growth. Hence, as the Cr layer is not fully saturated with carbon after 10 min, some of the available carbon will continue to dissolve into Cr instead of forming CNFs, and this is reflected in the observed lengths of the growing CNFs.

The presence of oxygen is expected to play a significant role in the evolution and distribution of phases at the Si-Ti and Si-Cr interfaces [21]. In our experiments, both Cr-Ni and Ti-Ni substrates were exposed to air between our processing steps. Hence we expect the substrates to be saturated with oxygen at room temperature. It should be noted that Ti has a higher affinity for oxygen than Cr [21]. From the ternary Ti-Si-O and Cr-Si-O phase diagrams, one can readily see that the thermodynamic stability of the interfaces is very different. Based on Fig. 7(a) and (b), local thermodynamic equilibrium is possible between Cr and SiO_2, whereas it is not the case with Ti and SiO_2 as in the former case there is a tie-line connecting the two phases directly, a feature that is missing in the Ti-Si-O phase diagram. This naturally means that from the thermodynamic point of view, Cr-SiO_2 interface is far more stable than Ti-SiO_2 where the formation of several additional phases is expected.

Richter et al. reported that when Ti starts to form $TiSi_2$, the oxygen that was initially contained in the consumed Ti region accumulates into the Ti film near the Ti-$TiSi_2$ interface. This phenomenon, commonly referred to as the “snowplow effect”, slows down and ultimately prevents the formation of further $TiSi_2$. In experiments done on a pure Si-Ti system (i.e. no Ni overlayer), it has been reported that oxygen accumulation leads to the formation of a Ti_5Si_3 interlayer between $TiSi_2$ and Ti [24]. This can be readily rationalized by the fact that out of the Ti-silicides only Ti_5Si_3 exhibits significant ternary oxygen solubility as well as can at the same time exist at local equilibrium with SiO_2. As our annealing time is rather short, we do not see the sequential formation predicted by the stable phase diagram in Fig. 7(b) but instead are dealing with local thermodynamic equilibrium [25]. Nevertheless, we can

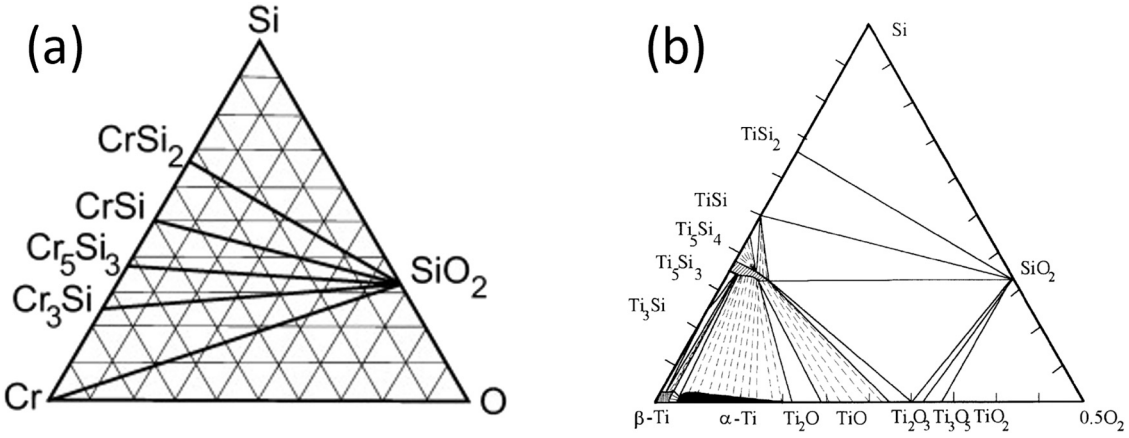

Fig. 7. Ternary phase diagram of Cr-Si-O system (T = 373–1273 K) (a), ternary phase diagram Ti–Si–O system at T = 1300 K (b). Reprinted from [22] (a), and [23] (b), with permission from Elsevier.

conclude that the inherently unstable Ti-SiO_2 interface will undergo interdiffusion and redistribution of species, as also shown in the TEM micrographs. As the solubility of oxygen to Ti is extremely high, and the driving force for the dissolution is high [26], it is likely that SiO_2 at the interface will also be mostly reduced and the resulting oxygen incorporated into the Ti-phase.

On the other hand, no redistribution of oxygen was reported during Cr-silicide formation under similar experimental conditions [21]. This behavior can again be rationalized based on the available ternary phase diagram (Fig. 7(a)), which shows, as discussed above, that local equilibrium exists between Cr and SiO_2. Thus, there is no need, from the thermodynamics of the system, to rearrange the phase at the interphasial area and therefore also the SiO_2 at the interface can be expected to stay intact. Note also that the solubility of oxygen in Cr is much smaller than that in Ti.

What are the consequences of the above discussion for our system? We can see that in the Cr-Ni layer structure, there is hardly any Ni at the interface (it is located exclusively at the tips of the fibers) whereas in Ti-Ni layer structure, there is a Ni-silicide phase between the Ti and S as shown by the TEM micrographs. It has been reported that the formation of NiSi is suppressed in the presence of a thin native oxide film (which is present in our samples) [27]. On the other hand, Lee et al. reported that the stability of NiSi is enhanced if Ti is incorporated in Ni thin films [28]. In their study, Ni silicidation reaction was observed at a significantly lower temperature due to the incorporation of Ti, and it was proposed that Ti reacts with interfacial SiO_2, resulting in the formation of a Ni-permeable diffusion membrane [28]. Again, this behavior is evident based on the phase diagrams in Fig. 7, which shows that because of the absence of local equilibrium between Ti and SiO_2 additional phases will form, and oxygen redistribution (partial or complete reduction of SiO_2) is inevitable as discussed above. This will then provide Ni feasible access to Si substrate and result in formation of Ni_xSi_{1-x} phase(s).

We used cyclic voltammetry (CV) to investigate the electrochemical properties of CNF samples. In this work, we focus on two important electrochemical parameters - analytical potential window and pseudocapacitance. Sulphuric acid is among the most widely used electrolytes in electroanalytical chemistry, while Phosphate Buffered Saline (PBS) is frequently used as an electrolyte in biosensing applications. Therefore, we determined the pseudocapacitance and analytical potential window of the CNFs in these two electrolytes. The effects of the dimensions of CNFs on the electron transfer kinetics were studied using an OSR probe $Ru(NH_3)_6Cl_3$ (in PBS), which is known to be insensitive to the surface chemistry of the electrodes [29].

The solvent window of an electrolyte is defined as the potential range between the oxygen evolution reaction (OER) and hydrogen evolution reaction (HER), which occur at the cathodic and anodic ends, respectively. From the electroanalytical point of view, it is more useful to define an analytical potential window where the analyte signal can be precisely measured, even though the exponential increase in current due to HER and OER is not yet seen. The analytical potential window is defined using a self-chosen threshold current value and is, by definition, narrower than the solvent window. We selected a threshold current density of ±150 μA/cm^2 for this purpose.

The analytical potential windows (Table 2) were determined with cyclic voltammetry in H_2SO_4 and in PBS. The cyclic voltammograms are presented in Fig. S5. Ti-Ni-CNFs possess larger potential windows than Cr-Ni-CNFs in both electrolytes for all CNF lengths. However, the difference between the potential windows of Ti-Ni-CNFs and Cr-Ni-CNFs was smaller in PBS in comparison to H_2SO_4, where Cr-Ni-CNFs and Ti-Ni-CNFs with varied lengths showed potential windows ranging from 1.02–1.42 to 1.23–1.54 V respectively. Cr-Ni-CNFs demonstrated a larger potential window in PBS compared to H_2SO_4, indicating better stability of the Cr-Ni-CNFs in a physiological saline environment. Contrary to Cr-Ni-CNFs, the potential windows of Ti-Ni-CNFs are approximately similar in both PBS and in H_2SO_4. Moreover, the width of the potential windows for Cr-Ni CNF decreased with an increase in fiber length.

Table 2
Analytical potential window, pseudocapacitance and outer sphere redox characteristics for CNF electrodes. Sample size = 3. ΔE_p and $I_{p,a}/I_{p,c}$ values were measured at a scan rate of 1 V/s.

Sample type	Analytical potential window (V)		Pseudocapacitance (μF/cm^2)		Outer Sphere Redox characteristics (scan rate = 1 V/s)	
	In H_2SO_4 pH 0.8	In PBS pH 7.4	In H_2SO_4 pH 0.8	In PBS pH 7.4	ΔE_p (mV)	$I_{p,a}/I_{p,c}$
Cr-Ni-CNF 1 min	1.16 ± 0.04	1.42 ± 0.01	372 ± 89	201 ± 13	59.9 ± 1.5	0.95 ± 0.01
Cr-Ni-CNF 5 min	0.98 ± 0.07	1.37 ± 0.02	416 ± 5	332 ± 7	N/A	N/A
Cr-Ni-CNF 10 min	1.03 ± 0.11	1.32 ± 0.07	547 ± 19	414 ± 2	N/A	N/A
Cr-Ni-CNF 30 min	0.72 ± 0.11	1.02 ± 0.25	894 ± 29	705 ± 117	53.2 ± 1.5	0.88 ± 0.04
Ti-Ni-CNF 1 min	1.33 ± 0.03	1.54 ± 0.03	263 ± 54	207 ± 20	60.6 ± 1.0	0.89 ± 0.01
Ti-Ni-CNF 5 min	1.45 ± 0.02	1.43 ± 0.02	286 ± 4	280 ± 22	N/A	N/A
Ti-Ni-CNF 10 min	1.56 ± 0.03	1.54 ± 0.04	255 ± 16	350 ± 60	N/A	N/A
Ti-Ni-CNF 30 min	1.33 ± 0.06	1.23 ± 0.09	397 ± 43	381 ± 19	53.2 ± 1.5	0.85 ± 0.02

Pseudocapacitance (C_{dl}) is a faradaic property that arises on electrode surfaces during electrochemical reactions, wherein due to thermodynamic reasons, charge q depends on potential, resulting in pseudocapacitance $C = d(\Delta q)/dV$ [30]. Several electrochemical processes contribute to pseudocapacitance, including adsorption, intercalation and surface redox reactions. We expect the pseudocapacitance to increase with the increase in CNF length as well as population density, since both these parameters increase the available surface area.

The pseudocapacitance of the electrical double layers of all electrodes was calculated from cyclic voltammograms recorded in blank PBS (pH 7.4) and in H_2SO_4 (pH 0.8) at different scan rates (10 mv/s–400 mV/s). The difference between anodic and cathodic current densities (defined from the measured current dividing it by the geometric area of the electrode) at different scan rates and the equation $\Delta i = 2 \times C \times v$ was used to determine the numerical value of the pseudocapacitance.

Cr-Ni-CNFs showed higher C_{dl} in H_2SO_4 than in PBS electrolyte, while C_{dl} for Ti-Ni-CNF electrodes is approximately similar in both electrolytes (Table 2). As expected, the C_{dl} of the electrodes increases with the increase in the length in both Cr-Ni and Ti-Ni systems, indicating the increase in the surface area. C_{dl} of 5- and 10-minute grown Ti-Ni-CNFs deviate from the trend. Nonetheless, C_{dl} of the longest CNFs is significantly larger than the shortest CNFs - about two times larger for Ti-Ni-CNFs and three times larger for Cr-Ni-CNFs. However, C_{dl} of the electrodes in Cr-Ni system is higher, indicating that the overall surface area, which is contributed by the population density, diameter and lengths of the fibers, is higher in comparison to Ti-Ni-CNFs. These results correlate with our analysis above, where we demonstrated that Cr-Ni-CNFs have greater population density, and therefore, greater surface area in comparison to Ti-Ni-CNFs. Overall, Cr-Ni-CNFs showed enhanced capacitance with a decrease in the potential window with respect to the increase in the fiber length. While length of the fibers did not influence the potential window of Ti-Ni-CNFs in any systematic way, C_{dl}, however, increased with the increase in fiber length.

Peak potential separation (ΔE_p) and the ratio of the oxidation to the reduction peak current ($I_{p,a}/I_{p,c}$) values at 1 V/s scan rate are shown in Table 2 for electrodes with the shortest and longest CNF lengths studied for both Cr-Ni and Ti-Ni interfaces. Based on these results, the electron transfer kinetics appear nearly reversible for all the electrodes. However, $I_{p,a}/I_{p,c}$ is closer to 1 for the CNFs with 1-minute growth in comparison to CNF with 30 min growth on both types of substrates. This indicates higher reversibility of the OSR redox reaction on electrodes with shorter fibers. Moreover, according to the ΔE_p values, the electron transfer kinetics appear slightly faster with the longest CNF in comparison to the shorter CNF on both interfaces. However, this may be caused by thin liquid layer formation, which will have a similar effect of reducing the ΔE_p values than higher heterogeneous electron transfer (HET) rates have. This phenomenon occurs at a certain ratio of the diffusion layer to surface feature thickness and is therefore dependent on both the fiber length and the scan rate. As the nanofiber lengths reach hundreds of nanometers, thin liquid layer formation is a feasible option in this system, especially in the case of the longest CNFs within the scan rates used in this study. A detailed study of the thin-liquid layer formation on these electrodes is presented in a separate work [29].

4. Conclusions

We have demonstrated that the interaction between the catalyst and adhesive layers plays a notable role in the growth behavior, the macroscale morphology of PECVD-grown CNFs and their electrochemical performance. Our results show that (1) Cr-Ni-CNFs have a larger population density than Ti-Ni-CNFs, (2) Ti-Ni-CNFs grow faster for the first 10 min of the growth process, however, both types of CNFs saturate to similar lengths after 30 min, and (3) the macroscale morphology of the CNFs can be used to tune their electrochemical properties. All these features can be rationalized by considering the interfacial interactions in the two systems. Owing to the inherent instability of the Ti-Ni interface at our process temperature, a portion of the Ni in the catalyst layer diffuses through Ti and forms a silicide. It is likely that oxygen redistribution also plays a role in the formation of Ni_xSi_{1-x} phases. As a result, a smaller amount of Ni is available for CNF nucleation, and therefore, Ti-Ni-CNFs have a smaller population density than their Cr-Ni counterparts. The stability of the Cr-Ni interface at our process temperature, on the other hand, results in a higher availability of Ni for CNF nucleation, and therefore, a larger population density of fibers. It is likely that the difference in the rate of growth between the two types of substrates is caused by the gradual dissolution of carbon into the thicker Cr layer. Further, we show that the macroscale geometry of fibers influences, for instance, the pseudocapacitance of CNF electrodes without significantly affecting the electron transfer kinetics. Thus, this study paves the way towards designing application-specific CNF electrodes by precisely controlling their macroscale morphology.

CRediT authorship contribution statement

Ishan Pande: Conceptualization, Methodology, Writing - Original draft preparation, Writing - Reviewing and Editing, Investigation, Resources, Visualization. **Laura Ferrer Pascual:** Investigation, Writing - Original draft preparation. **Ayesha Kousar:** Writing - Original draft preparation. **Emilia Peltola:** Funding acquisition, Writing - Review & Editing. **Hua Jiang:** Investigation. **Tomi Laurila:** Conceptualization, Methodology, Writing - Original draft preparation, Writing - Reviewing and Editing, Resources, Funding acquisition, Supervision.

Declaration of competing interest

The authors declare that they have no known competing financial interests or personal relationships that could have appeared to influence the work reported in this paper.

Data availability

Data will be made available on request.

Acknowledgments

This work was supported by funding from the Academy of Finland (#321996 and #328854) and Jane and Aatos Erkko Foundation. The authors acknowledge the provision of facilities and technical support by Aalto University at OtaNano - Nanomicroscopy Center (Aalto-NMC) and at Micronova Nanofabrication Centre. I.P. would like to thank Elli Leppänen and Petri Mustonen for discussions regarding the PECVD process, and Dr. Jani Sainio for help with sample characterization.

Appendix A. Supplementary data

Supplementary data to this article can be found online at https://doi.org/10.1016/j.diamond.2022.109566.

References

[1] S. Sainio, T. Palomäki, N. Tujunen, V. Protopopova, J. Koehne, K. Kordas, J. Koskinen, M. Meyyappan, T. Laurila, Integrated carbon nanostructures for detection of neurotransmitters, Mol. Neurobiol. 52 (2015) 859–866, https://doi.org/10.1007/s12035-015-9233-z.

[2] L.-F. Chen, Y. Feng, H.-W. Liang, Z.-Y. Wu, S.-H. Yu, Macroscopic-scale three-dimensional carbon nanofiber architectures for electrochemical energy storage devices, Adv. Energy Mater. 7 (2017), 1700826, https://doi.org/10.1002/aenm.201700826.

[3] Y. Shen, L. Li, K. Xiao, J. Xi, Constructing three-dimensional hierarchical architectures by integrating carbon nanofibers into graphite felts for water purification, ACS Sustain. Chem. Eng. 4 (2016) 2351–2358, https://doi.org/10.1021/acssuschemeng.6b00030.

[4] H. Lu, W. Fan, Y. Huang, T. Liu, Lotus root-like porous carbon nanofiber anchored with CoP nanoparticles as all-pH hydrogen evolution electrocatalysts, Nano Res. 113 (11) (2018) 1274–1284, https://doi.org/10.1007/S12274-017-1741-X.

[5] N. Isoaho, S. Sainio, N. Wester, L. Botello, L.S. Johansson, E. Peltola, V. Climent, J. M. Feliu, J. Koskinen, T. Laurila, Pt-grown carbon nanofibers for detection of hydrogen peroxide, RSC Adv. 8 (2018) 12742–12751, https://doi.org/10.1039/c8ra01703d.
[6] N. Isoaho, E. Peltola, S. Sainio, J. Koskinen, T. Laurila, Pt-grown carbon nanofibers for enzymatic glutamate biosensors and assessment of their biocompatibility, RSC Adv. 8 (2018) 35802–35812, https://doi.org/10.1039/C8RA07766E.
[7] N. Isoaho, E. Peltola, S. Sainio, N. Wester, V. Protopopova, B.P. Wilson, J. Koskinen, T. Laurila, Carbon nanostructure based platform for enzymatic glutamate biosensors, J. Phys. Chem. C 121 (2017) 4618–4626, https://doi.org/10.1021/acs.jpcc.6b10612.
[8] H. Cheng, Z. Zhou, Y. Li, W. Huang, J. Feng, T. Tang, L. Li, Electrochemiluminescence sensor based on electrospun three-dimensional carbon nanofibers for the detection of difenidol hydrochloride, Sensors 19 (2019) 3315, https://doi.org/10.3390/S19153315.
[9] X. Zhou, Y. Wang, C. Gong, B. Liu, G. Wei, Production, structural design, functional control, and broad applications of carbon nanofiber-based nanomaterials: a comprehensive review, Chem. Eng. J. 402 (2020), 126189, https://doi.org/10.1016/J.CEJ.2020.126189.
[10] K. Kamimura, Y. Matsumoto, O.O. Myo Than, M. Nakao, Y. Onuma, in: SEM and TEM observation of carbon nano-fibers prepared by hot filament assisted sputtering 340, 2006, pp. 713–717, https://doi.org/10.1080/10587250008025552.
[11] A.V. Melechko, V.I. Merkulov, T.E. McKnight, M.A. Guillorn, K.L. Klein, D. H. Lowndes, M.L. Simpson, Vertically aligned carbon nanofibers and related structures: controlled synthesis and directed assembly, J. Appl. Phys. 97 (2005), 041301, https://doi.org/10.1063/1.1857591.
[12] A.V. Melechko, V.I. Merkulov, D.H. Lowndes, M.A. Guillorn, M.L. Simpson, Transition between `base' and `tip' carbon nanofiber growth modes, Chem. Phys. Lett. 356 (2002) 527–533, https://doi.org/10.1016/S0009-2614(02)00406-2.
[13] A. Röthlisberger, M. Seita, A. Reiser, E. Shawat, R. Spolenak, G.D. Nessim, Investigating the mechanism of collective bidirectional growth of carbon nanofiber carpets on metallic substrates, Carbon 63 (2013) 498–507, https://doi.org/10.1016/J.CARBON.2013.07.025. N. Y.
[14] V.I. Merkulov, D.H. Lowndes, Y.Y. Wei, G. Eres, E. Voelkl, Patterned growth of individual and multiple vertically aligned carbon nanofibers, Appl. Phys. Lett. 76 (2000) 3555–3557, https://doi.org/10.1063/1.126705.
[15] C.W. Bale, E. Bélisle, P. Chartrand, S.A. Decterov, G. Eriksson, A.E. Gheribi, K. Hack, I.H. Jung, Y.B. Kang, J. Melançon, A.D. Pelton, S. Petersen, C. Robelin, J. Sangster, P. Spencer, M.A. Van Ende, FactSage thermochemical software and databases, 2010–2016, Calphad 54 (2016) 35–53, https://doi.org/10.1016/J.CALPHAD.2016.05.002.
[16] Z. He, J.L. Maurice, A. Gohier, C.S. Lee, D. Pribat, C.S. Cojocaru, Iron catalysts for the growth of carbon nanofibers: Fe, Fe 3C or both? Chem. Mater. 23 (2011) 5379–5387, https://doi.org/10.1021/CM202315J/SUPPL_FILE/CM202315J_SI_001.PDF.
[17] G. Bin Zheng, K. Kouda, H. Sano, Y. Uchiyama, Y.F. Shi, H.J. Quan, A model for the structure and growth of carbon nanofibers synthesized by the CVD method using nickel as a catalyst, Carbon 42 (2004) 635–640, https://doi.org/10.1016/J.CARBON.2003.12.077. N. Y.
[18] S. Helveg, C. López-Cartes, J. Sehested, P.L. Hansen, B.S. Clausen, J.R. Rostrup-Nielsen, F. Abild-Pedersen, J.K. Nørskov, Atomic-scale imaging of carbon nanofibre growth, Nature 427 (2004) 426–429, https://doi.org/10.1038/nature02278.
[19] T. Laurila, J. Molarius, Reactive phase formation in thin film metal/metal and metal/silicon diffusion couples, Crit. Rev. Solid State Mater. Sci. 28 (2003) 185–230, https://doi.org/10.1080/10408430390261955.
[20] T. Tokunaga, K. Nishio, H. Ohtani, M. Hasebe, Thermodynamic assessment of the Ni–Si system by incorporating ab initio energetic calculations into the CALPHAD approach, Calphad 27 (2003) 161–168, https://doi.org/10.1016/S0364-5916(03)00049-X.
[21] H. Jiang, H.J. Whitlow, M. Östling, E. Niemi, F.M. D'Heurle, C.S. Petersson, A quantitative study of oxygen behavior during CrSi2 and TiSi2 formation, J. Appl. Phys. 65 (1998) 567, https://doi.org/10.1063/1.343143.
[22] N.I. Matskevich, Z.I. Semenova, Phase transformations in the system Cr–Si–W–O, J. Alloys Compd. 509 (2011) 6146–6151, https://doi.org/10.1016/J.JALLCOM.2011.03.024.
[23] E.V. Shalaeva, S.V. Borisov, O.F. Denisov, M.V. Kuznetsov, Metastable phase diagram of Ti–Si–N(O) films (CSi<30 at.%), Thin Solid Films 339 (1999) 129–136, https://doi.org/10.1016/S0040-6090(98)01259-0.
[24] F. Richter, E. Bugiel, H.B. Erzgräber, D. Panknin, Formation of titanium silicide during rapid thermal annealing: influence of oxygen, J. Appl. Phys. 72 (1998) 815, https://doi.org/10.1063/1.351821.
[25] A. Paul, T. Laurila, V. Vuorinen, S.V. Divinski, Thermodynamics, Diffusion And the Kirkendall Effect in Solids, Springer International Publishing, Cham, 2014, https://doi.org/10.1007/978-3-319-07461-0.
[26] E. Fromm, Gase und Kohlenstoff in Metallen, Angewandte MetallkundeBd. 26, Springer-Verlag, 1976.
[27] P.S. Lee, D. Mangelinck, K.L. Pey, J. Ding, J.Y. Dai, C.S. Ho, A. See, On the Ni–Si phase transformation with/without native oxide, Microelectron. Eng. 51–52 (2000) 583–594, https://doi.org/10.1016/S0167-9317(99)00521-3.
[28] R.T.P. Lee, D.Z. Chi, M.Y. Lai, N.L. Yakovlev, S.J. Chua, Effects of Ti incorporation in Ni on silicidation reaction and structural/electrical properties of NiSi, J. Electrochem. Soc. 151 (2004) G642, https://doi.org/10.1149/1.1782634/XML.
[29] L.F. Pascual, I. Pande, A. Kousar, S. Rantataro, T. Laurila, Nanoscale engineering to control mass transfer on carbon-based electrodes, Electrochem. Commun. 140 (2022), 107328, https://doi.org/10.1016/J.ELECOM.2022.107328.
[30] B.E. Conway, V. Birss, J. Wojtowicz, The role and utilization of pseudocapacitance for energy storage by supercapacitors, J. Power Sources 66 (1997) 1–14, https://doi.org/10.1016/S0378-7753(96)02474-3.